




Carbon-film-based Zernike phase plates with smooth thickness gradient for phase-contrast transmission electron microscopy with reduced fringing artefacts

M. Obermair¹  | S. Hettler^{1,2}  | M. Dries¹ | M. Hugenschmidt^{1,3}  |
R. Spiecker^{1,4} | D. Gerthsen^{1,3}

¹Laboratory for Electron Microscopy (LEM), Karlsruhe Institute of Technology (KIT), Karlsruhe, Germany

²Laboratorio de Microscopías Avanzadas (LMA), Instituto de Nanociencia y Materiales de Aragón (INMA), Universidad de Zaragoza, Zaragoza, Spain

³3DMM2O – Cluster of Excellence (EXC-2082/1–390761711), Karlsruhe Institute of Technology (KIT), Karlsruhe, Germany

⁴Laboratory for Applications of Synchrotron Radiation (LAS), Karlsruhe Institute of Technology (KIT), Karlsruhe, Germany

Correspondence

M. Obermair, Laboratory for Electron Microscopy (LEM), Karlsruhe Institute of Technology (KIT), Engesserstraße 7, 76131 Karlsruhe, Germany.
Email: martin.obermair@kit.edu

Funding information

European Union's Horizon 2020 research and innovation program under the Marie Skłodowska-Curie grant, Grant/Award Number: 889546; Carl-Zeiss-Stiftung, Grant/Award Number: 10.13039/100007569; Deutsche Forschungsgemeinschaft, Grant/Award Numbers: Ge 841/26, Germany's Excellence Strategy-2082/1-39076, HE 7675/1-1

Abstract

Phase plates (PPs) in transmission electron microscopy (TEM) improve the contrast of weakly scattering objects under in-focus imaging conditions. A well-established PP type is the Zernike (Z)PP, which consists of a thin amorphous carbon (aC) film with a microscaled hole in the centre. The mean inner potential of the aC film is exploited to shift the phase of the scattered electrons while the unscattered electrons in the zero-order beam propagate through the hole and remain unaffected. However, the abrupt thickness increase at the hole edge induces an abrupt change of the phase-shift distribution and leads to fringing, that is, intensity oscillations around imaged objects, in TEM images. In this work, we have used focused-ion-beam milling to fabricate ZPPs with abrupt and graded thickness profiles around the centre hole. Depending on the thickness gradient and inner hole radius, graded-ZPP-TEM images of an aC/vacuum interface and bundles of carbon nanotubes (CNTs) show strongly reduced fringing. Image simulations were performed with ZPP-phase-shift distributions derived from measured thickness profiles of graded ZPPs, which show good agreement with the experimental images.

- Fringing artefacts, that is, intensity oscillations around imaged objects, are strongly reduced for Zernike phase plates with a graded thickness profile around the centre hole.
- Focused-ion-beam milling is used to fabricate graded Zernike phase plates with specific inner hole radius and thickness gradients.
- The phase-shift distribution is obtained from measured thickness profiles around the centre hole.
- Image simulations based on experimentally measured thickness/phase-shift distributions show good agreement with experimental Zernike phase-plate TEM images.

This is an open access article under the terms of the [Creative Commons Attribution-NonCommercial-NoDerivs](https://creativecommons.org/licenses/by-nc-nd/4.0/) License, which permits use and distribution in any medium, provided the original work is properly cited, the use is non-commercial and no modifications or adaptations are made.

© 2022 The Authors. *Journal of Microscopy* published by John Wiley & Sons Ltd on behalf of Royal Microscopical Society.

KEYWORDS

carbon nanotubes (CNTs), fringing artefact, image simulations, phase-contrast TEM, thin amorphous carbon film, transmission electron microscopy (TEM), Zernike phase plate (ZPP)

1 | INTRODUCTION

Weak contrast is an obstacle for transmission electron microscopy (TEM) imaging of organic materials because their chemical constituents mainly have low atomic numbers and interact only weakly with high-energy electrons. This causes only a weak modulation of the phase of the electron wave and the modulation of its amplitude is even lower. Thus, organic materials are often almost invisible in conventional (C) TEM images under in-focus conditions. Until today, defocusing of the objective lens is the most established technique to improve the contrast of such weak-phase objects. However, defocus is accompanied by the degradation of resolution and image interpretability.¹

Apart from defocusing, the generation of phase contrast is enabled by the application of a physical phase plate (PP) under in-focus conditions by inducing a relative phase shift between the scattered and unscattered part of the electron wave in the back focal plane (BFP) of the objective lens. Optimum phase contrast of weak-phase objects is achieved with a relative phase shift of $\pm \pi/2$. Among the numerous PP designs^{2,3} that can be coarsely subdivided into thin-film, laser,^{4,5} and electrostatic approaches, the well-known Zernike (Z) PP⁶ for applications in light microscopy was the first PP established in TEM.^{7,8}

The ZPP consists of a thin amorphous carbon (aC) film with a microstructured hole in the centre of the film, as illustrated in the schematic drawing in Figure 1A. Due to the mean inner potential (MIP) of the aC film, the ZPP shifts the phase of the scattered electrons, while the unscattered electrons propagate through the microstructured hole and remain unaffected. The phase shift φ_{PP} imposed by the aC film of the ZPP can be calculated from the following equation:⁹

$$\varphi_{PP} = \frac{\pi}{\lambda U} \cdot \frac{1 + 2\alpha U}{1 + \alpha U} \cdot V_0 \cdot t. \quad (1)$$

The equation depends on the MIP V_0 of the PP material (e.g. 9.0 V for aC¹⁰), the electron wavelength λ , the acceleration voltage U given in units of Volts, the constant $\alpha = 0.9788 \cdot 10^{-6} \frac{1}{V}$, and the thickness t of the aC film. The optimal phase shift of $\pi/2$ can be adjusted during the fabrication process of the thin film by choosing its thickness t according to Equation (1).

Although the concept of a ZPP is easy to implement, it is associated with some disadvantages that partly affect

the image quality. For instance, the aC film degrades after a few hours of use and needs to be replaced frequently. The irradiation at room temperature with high-energy electrons causes contamination and electrostatic charging. Both effects influence the phase-shift properties and lead to artefacts in ZPP-TEM images. A thorough understanding of these effects is the subject of current research.^{11–14} The operation time of the ZPP can be extended by using a heating device to keep the aC film at an elevated temperature to counteract contamination.¹⁵ Furthermore, recent publications report on the possibly extended durability of ZPPs fabricated from alternative materials, for example, Si or metallic glasses.^{16,17}

Another drawback of the ZPP is that phase contrast is limited to objects below a maximum size because the radius of the microstructured hole in the thin film determines the cut-on frequency. Furthermore, the abrupt onset of the phase shift at the edge of the hole induces fringing artefacts, that is, image-intensity oscillations around imaged objects that significantly impede image interpretability.¹⁸ Computational methods to correct fringing to a certain degree have been proposed by Danev et al.^{19,20} Furthermore, an experimental study shows a

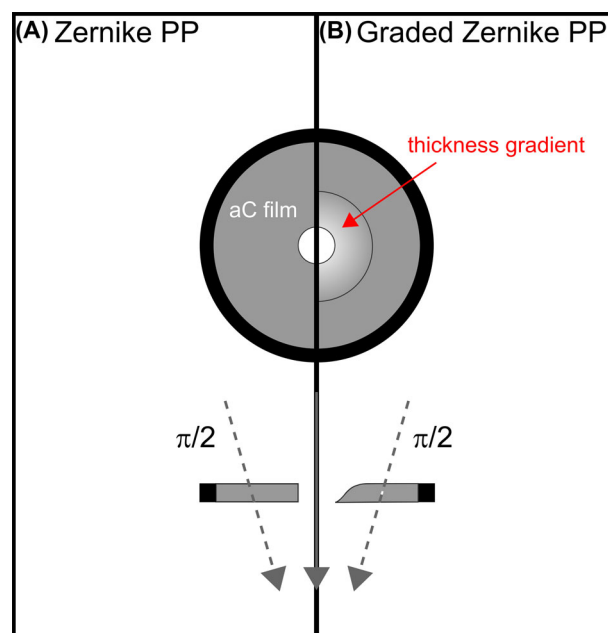


FIGURE 1 Schematic illustration of (A) a ZPP and (B) a graded ZPP with a thickness gradient. The ZPPs are located in the back focal plane of the objective lens

significant reduction of fringing in time-averaged images obtained with a zero-order beam (ZOB) continuously rotating inside the ZPP hole.²¹

This work is concerned with an alternative approach to reduce fringing in ZPP TEM images. We present TEM images acquired with aC-film-based graded ZPPs, which are fabricated with a smooth thickness gradient at the edge of the hole (cf. scheme Figure 1B). The replacement of the abrupt thickness onset with a thickness gradient results in a smooth phase-shift profile. The reduction of fringing by different graded ZPPs is studied at the edge of an aC test specimen. Phase-contrast TEM imaging with graded ZPPs is demonstrated for bundles of carbon nanotubes (CNT), which show strong contrast enhancement and reduced fringing. Experimental results are confirmed by corresponding image simulations.

2 | MATERIALS AND METHODS

2.1 | ZPP fabrication

For the fabrication of the ZPPs, a thin aC layer was deposited on a freshly cleaved mica sheet (Plano, Wetzlar, Germany, Product No. 54) using electron-beam evaporation (PVD75, Kurt J. Lesker Company, Hastings, UK) of a graphitic carbon target. The aC film was subsequently floated off the mica in a distilled-water bath and placed on a TEM gold grid (Plano, Wetzlar, Germany, Product No. G2150A, 150 mesh). The thickness of the aC film was measured to be ~ 27 nm by thickness monitoring throughout the deposition process and additionally verified by cross-section TEM imaging. This thickness leads to a phase shift of -0.56π at 200 keV according to Equation (1).

Conventional and graded ZPP holes were structured by focused-ion-beam (FIB) milling of the aC film with the Ga-ion beam of a Helios G4 FX SEM/FIB dual-beam instrument (Thermo Fisher Scientific, Waltham, MA, USA) operated with a Ga-ion energy of 30 keV and a FIB current of 7 pA. The same instrument is equipped with a scanning transmission electron microscopy (STEM) detector, which was used to image the fabricated ZPPs with STEM-in-SEM. The conventional ZPP holes with abrupt hole edges were milled using circular FIB patterns with radii of 375 and 500 nm and scan direction 'inner to outer'. The graded ZPP holes were milled using a custom FIB routine, which is based on a 'stream file' that contains a chronologically ordered list of spatial coordinates and corresponding dwell times for the FIB patterning (cf. Supplementary Information Figure S1).

Graded ZPPs were structured in three sizes:

- Inner hole radius of 375 nm and an outer hole radius of 500 nm (375/500 nm, cf. Figure 2A),

- Inner hole radius of $0.5\ \mu\text{m}$ and an outer hole radius of $1.5\ \mu\text{m}$ ($0.5/1.5\ \mu\text{m}$, cf. Figure 2B) and
- Inner hole radius of $0.6\ \mu\text{m}$ and an outer hole radius of $1.5\ \mu\text{m}$ ($0.6/1.5\ \mu\text{m}$, cf. Figure 2C).

To determine the thickness profile of the fabricated graded ZPPs, high-angle annular dark-field (HAADF) STEM was performed at 30 keV in the Helios G4 FX (cf. Figure 2D–F). For small aC-film thicknesses, the image intensity in HAADF-STEM images increases linearly with the film thickness.²² This is the prerequisite for the determination of thickness profiles in Figure 2G–I obtained from intensity profiles along the dashed lines in Figure 2D–F. After subtracting the average vacuum intensity, the mean intensity of the unstructured aC film is calibrated by the measured thickness of ~ 27 nm. The green thickness profile of the graded ZPP (375/500 nm) in Figure 2G shows an abrupt step of ~ 11 nm directly at the inner hole radius, followed by a thickness increment of ~ 16 nm over a width of 125 nm (thickness gradient 0.128). The abrupt step of ~ 4 nm in the blue thickness profile (cf. Figure 2H) at the inner hole radius of the graded ZPP ($0.5/1.5\ \mu\text{m}$) is significantly smaller. The following thickness increment is approximately linear with an increase of ~ 23 nm over a width of $1\ \mu\text{m}$ (thickness gradient of 0.023). Thus, the thickness gradient of the graded ZPP ($0.5/1.5\ \mu\text{m}$) in Figure 2H is an order of magnitude smaller than the one of the graded ZPP (375/500 nm) in Figure 2G. Moreover, the blue thickness profile in Figure 2H shows a kink in the curve at the transition from the 4-nm step to the linear thickness gradient. The yellow thickness profile of the graded ZPP ($0.6/1.5\ \mu\text{m}$) in Figure 2I with a slightly larger hole (inner radius of $0.6\ \mu\text{m}$) and a narrower thickness gradient ($0.9\ \mu\text{m}$ in width) is similar to the blue profile. However, an abrupt change of the gradient does not occur yielding a rather smooth thickness increase of ~ 27 nm over a width of $0.9\ \mu\text{m}$ (thickness gradient of 0.03).

2.2 | Samples, PP implementation and experimental procedures

The ZPPs were mounted onto a customised PP holder equipped with a temperature sensor as described in Ref. (23), which can be heated to temperatures up to 200°C . A piezo-driven Kleindiek MM3A-EM micromanipulator system (Kleindiek, Reutlingen, Germany) was used to implement and move the PP holder with nanometre accuracy in the BFP of a Philips CM200 FEG/ST transmission electron microscope with a spherical aberration coefficient C_s of 1.2 mm and a field-emission gun operated at 200 kV. The PP holder was continuously heated to 160°C to prevent contamination of the ZPPs as suggested in Ref. (15). Vacuum

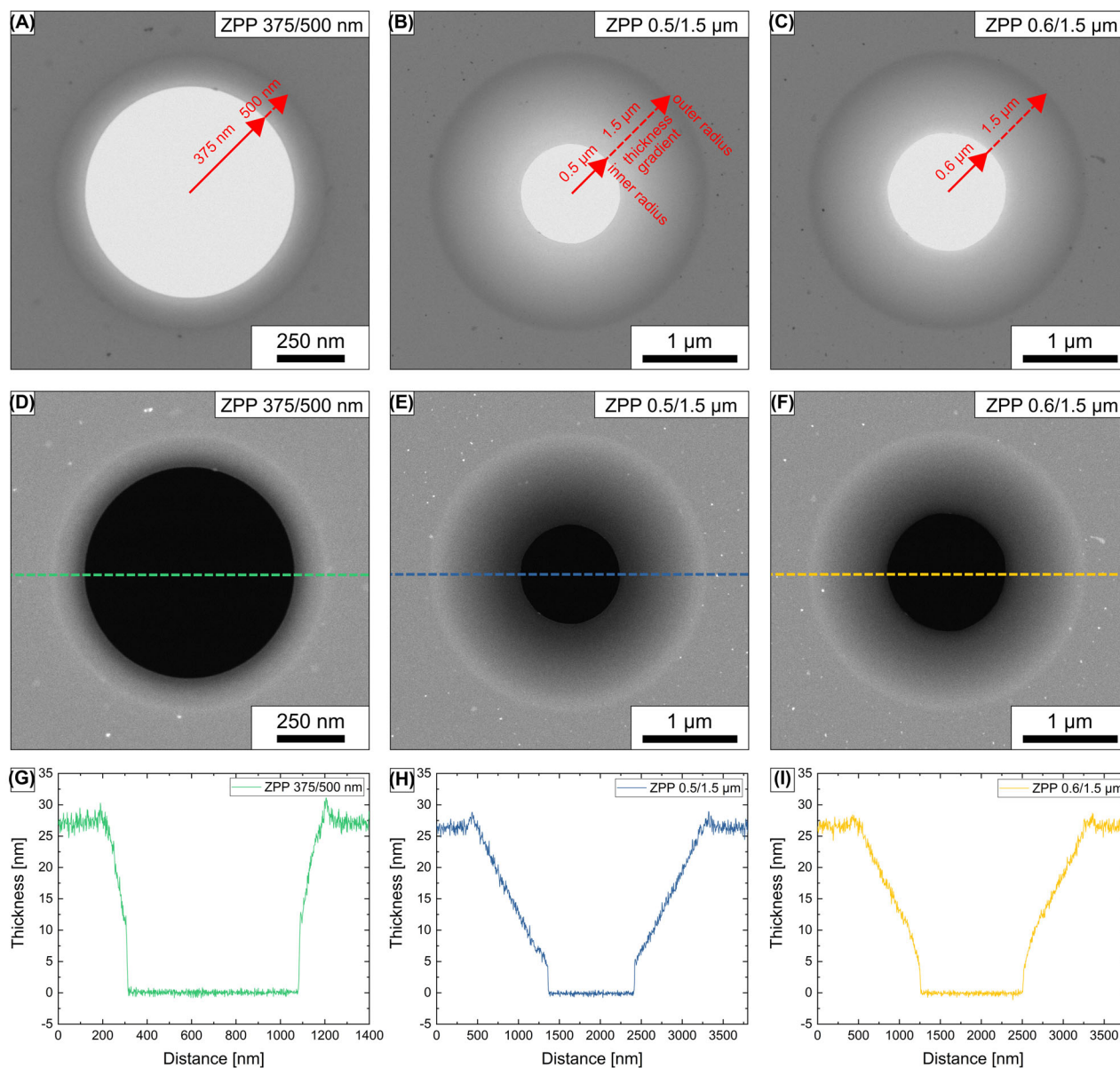


FIGURE 2 30 keV STEM images and thickness profiles of graded ZPPs. BF-STEM images of graded ZPPs with (A) an inner hole radius of 375 nm and an outer hole radius of 500 nm (375/500 nm), (B) an inner hole radius of 0.5 μm and an outer hole radius of 1.5 μm (0.5/1.5 μm) and (C) an inner hole radius of 0.6 μm and an outer hole radius of 1.5 μm (0.6/1.5 μm). HAADF-STEM images of the same graded ZPPs as in the images above (D) 375/500 nm, (E) 0.5/1.5 μm and (F) 0.6/1.5 μm . Thickness profiles (G) along the green dashed line in D, (H) along the blue dashed line in E and (I) along the yellow dashed line in F

conditions in the sample and PP region in the microscope were improved by using a liquid-nitrogen-cooled anticontamination device.

Due to the heating of the ZPPs in the microscope during operation, only temporary image-distorting charging effects after several minutes of intense illumination of the ZPP were observed. If charging occurred, another ZPP was used (the aC film contained four ZPPs with the same hole properties). Charging typically disappears over night by continuous heating of the aC film or after a cryocycle.

Thus, the ZPPs could be used for several months without degradation of the imaging quality.

The alignment of the ZPPs and setup of illumination conditions was carried out in the diffraction mode. The ZPPs were adjusted under on-plane conditions, where the BFP and the PP plane coincide. Due to the lack of space between the objective-lens pole pieces, the ZPP cannot be moved in z-direction. The on-plane condition is thus set up by changing the condenser-lens while being in diffraction mode. At first, the selected ZPP hole is centred roughly

around the zero-order beam (ZOB). Subsequently, the edge of the ZPP hole is focused using the diffraction focus. Finally, the condenser-lens system is adjusted such that the ZOB appears as small and round as possible, and the micro-manipulator is used to position the ZPP hole concentrically around the ZOB. The radius of the ZOB was ~ 50 nm.²³ We note that the positioning of graded ZPPs is not straightforward because the aC film is very thin at the hole edges and thus difficult to recognise in diffraction mode. For fine adjustment of graded ZPPs, we used fast Fourier transformations (FFTs) of acquired live-view images in TEM imaging mode.

For imaging, a TVIPS F416 (TVIPS, Gauting, Germany) CMOS camera was used. Fringing induced by conventional and graded ZPPs was analysed at the aC-film/vacuum interface of a test specimen. Bundles of single-walled carbon nanotubes (CNTs) were also used for phase-contrast TEM. The CNTs were prepared by laser evaporation of a composite carbon/nickel catalyst target (Tōyō Tanso, Osaka, Japan) and subsequently dispersed on a holey carbon film (Plano, Product No. S147-2).

2.3 | Image processing and simulations

Image parameters (defocus, phase shift) of experimental ZPP-TEM images were verified using a MATLAB program (The Mathworks, Natick, MA, USA)²⁴ that simulates a database of power spectra with different defocus, astigmatism and phase-shift values. Comparison of simulated power spectra with power spectra of experimental images returns the best-fitting parameters.²⁵ Spatial frequencies below the cut-on frequency q_c were not considered for parameter determination, as they are not phase-shifted by the aC film of the ZPP. The cut-on frequency was calculated from the ZPP-hole radius r by

$$q_c = \frac{r}{\lambda f}, \quad (2)$$

where f is the focal length of the objective lens (1.7 mm in our case). For PP-TEM images taken with a graded ZPP, spatial frequencies below the outer ZPP radius were excluded for parameter determination to avoid miscalculation due to the phase-shift gradient.

Intensity profiles were extracted from experimental images for comparison with simulated data. The intensity profiles were typically averaged over a width of 24 nm (images of aC film) and 12 nm (images of CNT bundles) for noise reduction.

We performed PP-TEM image simulations based on model object exit-wave functions (OWFs) of a holey aC film and a CNT bundle to obtain an improved under-

standing of the phase-contrast formation and fringing artefacts induced by the application of conventional and graded ZPPs. The OWFs are described by a function $A(x, y) \exp(i\phi(x, y))$ with amplitude A and a thickness-dependent phase shift ϕ . To determine the phase shift of the holey aC film, an analogous procedure was used as for the determination of the thickness profiles of the graded ZPP (see Supplementary Information for further details).

Based on the thickness measurements in Figure S2, one-half of the OWF of the aC film (cf. color-coded phase of OWF in Figure 3A) was defined as 10-nm-thick aC film, whereas the other half was defined as vacuum region. The phase shift ϕ of the 10-nm-thick aC film was calculated from Equation (1) with a MIP of 9 V^{10} resulting in a phase shift of 0.21π ($0.021 \pi/\text{nm}$). At the aC-film/vacuum interface, a smooth phase transition was defined in the OWF according to the measured thickness profile in Figure S2C. The transition extends smoothly over ~ 2 nm (for the simulation in Figure 4E) and ~ 4 nm (for the simulation in Figure 4F) to avoid an abrupt phase edge in the OWF and achieve good agreement with the experimental ZPP-TEM images. An additional narrow vacuum region and a graded decrease of the aC-film thickness were also defined on the left side of the aC film to avoid simulation artefacts due to non-periodic boundary conditions. Additionally, we assumed a slightly reduced amplitude $A = 0.99$ to model the observed intensity reduction in the images of the aC film. The phase of the OWF of a CNT bundle is shown in Figure 3B. It is modelled in a simplified way by a homogeneous cylinder with a radius of 7.5 nm and a MIP of 6 V .^{23,26} The projected phase $\phi(x)$ of the cylinder is calculated by $\phi(x) = 2\rho \sqrt{r_c^2 - x^2} \sqrt{r_c^2 - x^2}$ with the radius r_c and the phase shift per unit length $\rho = 0.014\pi/\text{nm}$ according to Equation (1). Density variations of the aC thin film were reflected by adding a random signal with a maximum phase shift of 0.04π and a maximum amplitude of 0.02 to the aC regions of the OWF.

For TEM image simulations, the image wave function was calculated by multiplying the Fourier transform of the OWF by the contrast-transfer function (CTF), the spatial coherence envelope function, and the aperture function. The CTF is given by $\exp(-i\chi)$ with the overall phase shift

$$\chi = \pi \Delta f \lambda q^2 + \frac{\pi}{2} C_s \lambda^3 q^4 + \varphi_{\text{PP}}(q) \quad (3)$$

with the defocus Δf . The spatial-frequency-dependent phase-shift distribution of the conventional ZPP φ_{PP} is defined as $\pi/2$ for $q > q_c$ and 0 for $q \leq q_c$. For the graded ZPPs, we determined the experimental phase-shift distributions shown in Figure 3C–E by converting the HAADF STEM images in Figure 2D–F into thickness maps and calculating the corresponding phase-shift values according to

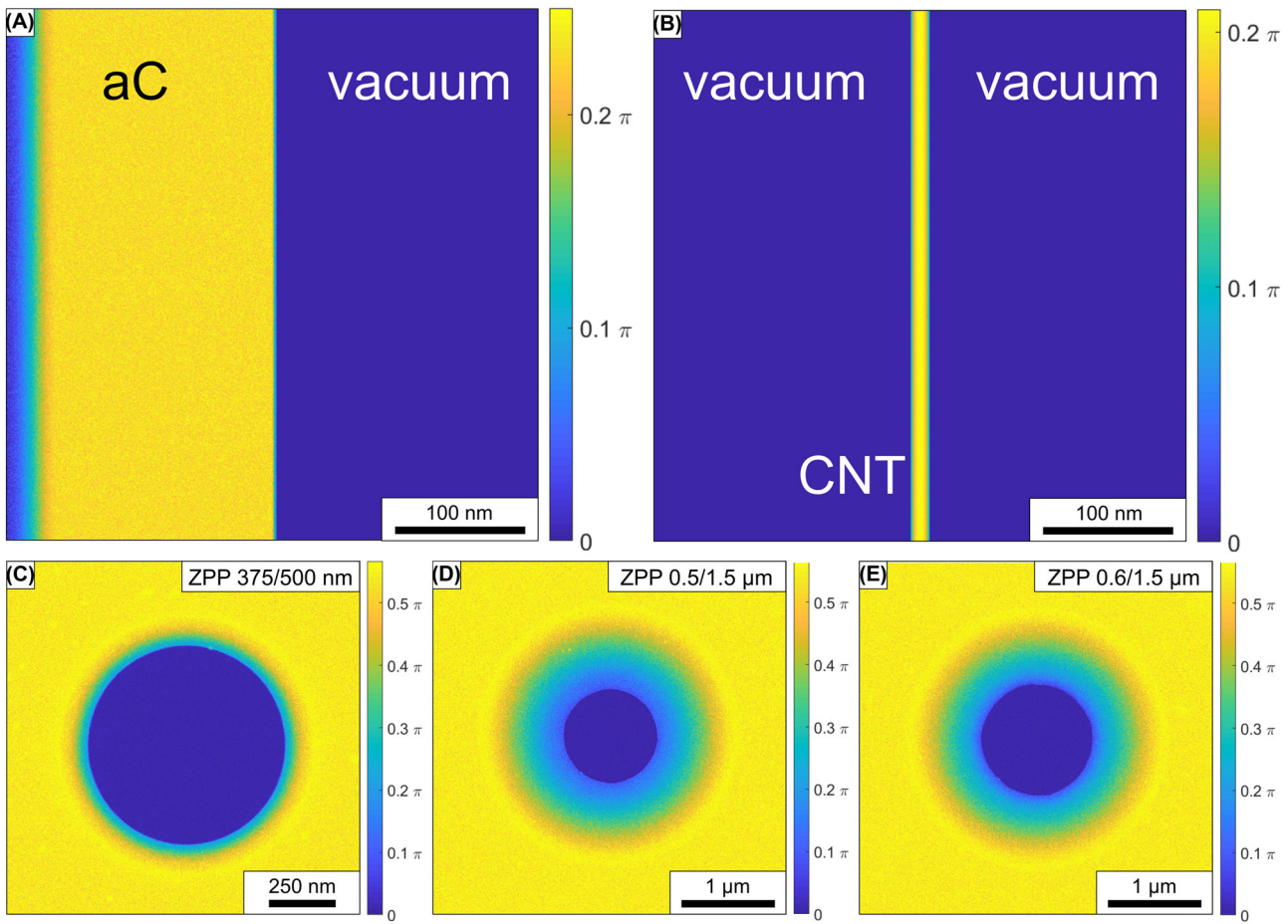


FIGURE 3 Color-coded phase distribution of the model OWF (A) of the aC/vacuum interface region and (B) of a CNT bundle in vacuum. Experimentally determined color-coded phase-shift distributions of the graded ZPPs (C) 375/500 nm, (D) 0.5/1.5 μm and (E) 0.6/1.5 μm

Equation (1) with a MIP of 9V.¹⁰ Amplitude damping by additional scattering in the aC film of ZPPs was also considered by calculating the damping factor $D = \exp(-\frac{t}{\lambda_{\text{el}}}) \cdot \exp(-\frac{t}{\lambda_{\text{inel}}})$, with the elastic and inelastic mean free path $\lambda_{\text{el}} = 262 \text{ nm}$ and $\lambda_{\text{inel}} = 155 \text{ nm}$ ²⁷ for the film thickness $t = 27 \text{ nm}$, which results in a damping factor of $D = 0.76$. The image intensity was obtained by inverse Fourier transformation and calculation of the absolute square of the image wave function. Partial temporal coherence was taken into account by using the weighted-focal-series method.²⁸ The finite radius of the ZOB ($\sim 50 \text{ nm}$) was taken into account in the image simulations by simulating images with a slightly decentred ZPP in the BFP. These images were incoherently summed up using Gaussian weighting factors. More information on details on PP TEM simulations and the importance of a finite ZOB radius on the image contrast is given in Ref. (29). Random noise (1 %) was added to the final images to model the noise of the camera, which was chosen to be small to better visualise the effect of the PP. The images were simulated at a large electron dose, that

is, without shot noise for the same reason. The custom MATLAB-based simulation software was published in previous work³⁰ and used with adapted functions for the simulation of graded ZPPs.

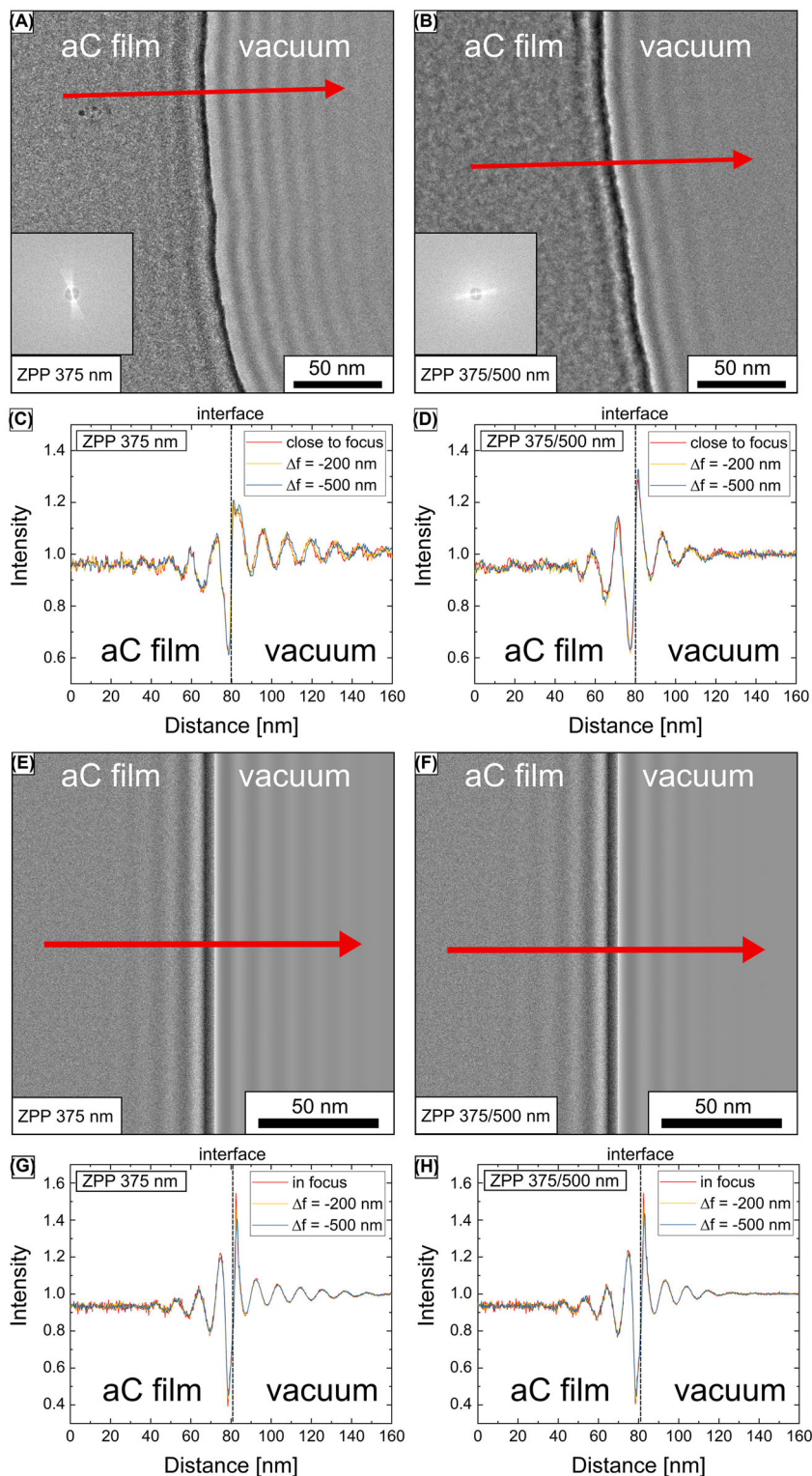
3 | RESULTS AND DISCUSSION

Section 3 is subdivided into two parts. In section 3.1, we present a general analysis of the effect of graded ZPPs on fringing artefacts at the aC-film/vacuum interface. Section 3.2 focuses on the imaging of CNT bundles as an example for nanoscaled objects.

3.1 | Analysis of fringing artefacts in graded-ZPP-TEM images at the aC-film/vacuum interface

Figure 4 compares phase-contrast TEM images obtained close to focus with a conventional ZPP (hole radius 375 nm)

FIGURE 4 Experimental and simulated ZPP-TEM images of an aC-film/vacuum-interface region and corresponding intensity line profiles. Experimental ZPP-TEM images taken close to focus with (A) a conventional ZPP with a hole radius of 375 nm and (B) a graded ZPP with a hole radius of 375/500 nm including corresponding power spectra. (C, D) Intensity line profiles along the red arrows in the corresponding experimental TEM images A and B. Simulated in-focus ZPP-TEM images for (E) a conventional ZPP with a hole radius of 375 nm and (F) a graded ZPP with a hole radius of 375/500 nm. (G, H) Intensity line profiles along the red arrows in the corresponding simulated TEM images E and F. The yellow and blue lines in C and D and G and H correspond to intensity line profiles obtained at the same sample area from PP-TEM images taken with a defocus of -200 nm and -500 nm. The intensity profiles are normalised with respect to the mean vacuum intensity in the corresponding image



in Figure 4A, a graded ZPP (hole radius 375/500 nm) in Figure 4B. Strong fringing is observed to originate at the edge of the aC film in Figure 4A. Figure 4C shows intensity profiles along the red arrow in Figure 4A from images taken at the same position with three different defocus values. The interface position is marked by a dashed black

line. All presented intensity profiles are normalised with respect to the mean vacuum intensity in the images. The red profile from the close-to-focus image visualises that fringing spreads out asymmetrically from the interface into the aC and vacuum regions. The profile shows seven maxima in the vacuum region and five minima in the aC

film with intensities that decrease with increasing distance from the film edge. The distance between adjacent maxima or minima is 11.5 nm, corresponding to a spatial frequency of 0.087 nm^{-1} . The fringe distance correlates with the cut-on frequency of 0.088 nm^{-1} of the conventional ZPP with a 350-nm hole radius (cf. Equation 2). The yellow and blue intensity profiles, obtained with Δf values of -200 nm and -500 nm , hardly differ from the red close-to-focus profile. This shows that Fresnel fringes at object boundaries in defocused TEM images are weak in comparison to fringing induced by the ZPP, at least for small Δf values below -500 nm . Fringing is also observed in the close-to-focus phase-contrast TEM image obtained with the graded ZPP (Figure 4B). However, the intensity oscillations decay faster with increasing distance from the interface compared to Figure 4A. This effect can be attributed to the thickness gradient of the graded ZPP as demonstrated by the red close-to-focus intensity profile in Figure 4D, taken along the red arrow in Figure 4B. It shows only four intensity maxima in the vacuum region and three intensity minima in the aC film. Again, the intensity profiles do not differ significantly for Δf values of -200 and -500 nm (yellow and blue curves).

Image simulations based on the aC/vacuum OWF in Figure 3A are presented in Figure 4E and F under in-focus conditions. The simulated image for a conventional ZPP with a hole radius of 375 nm in Figure 4E shows strong fringing while a faster decay of fringing is observed in the simulated image for the graded ZPP with a 375/500 nm hole radius in Figure 4F. Intensity line profiles along the red arrows in Figure 4E and F are shown in Figure 4G and H (red curves in-focus condition, yellow and blue curves at $\Delta f = -200 \text{ nm}$ and -500 nm) and agree well with the experimental intensity profiles in Figure 4C and D. The reduction of fringing by a graded ZPP with a radius of 375/500 nm is obvious but does not lead to the disappearance of fringing because the thickness gradient of 0.128 is still pronounced. Moreover, there is still an abrupt thickness step of $\sim 11 \text{ nm}$ at the inner hole radius of the ZPP (cf. Figure 2G), which causes fringing artefacts.

In Figure 5, we follow the same approach as in Figure 4 and analyse the fringing of a conventional and two graded ZPPs with a slightly larger hole radius and shallower thickness gradients. Figure 5A–C show phase-contrast TEM images taken close to focus with a conventional ZPP (hole radius $0.5 \mu\text{m}$, Figure 5A), a graded ZPP with a hole radius of $0.5/1.5 \mu\text{m}$ (Figure 5B), and a graded ZPP with a hole radius of $0.6/1.5 \mu\text{m}$ (Figure 5C). As expected, Figure 5A shows strong fringing emanating from the aC-film/vacuum interface. The red intensity profile in Figure 5D, taken along the red arrow in Figure 5A, reveals a fringing periodicity of 8 nm corresponding to a spatial frequency of 0.125 nm^{-1} . This agrees well with the cut-

on frequency of 0.117 nm^{-1} of the conventional ZPP with a $0.5 \mu\text{m}$ hole radius. The relative intensity of the fringes in Figure 5A and D is similar to Figure 3A and C and the same number of fringe maxima and minima is observed. However, the increase of the inner hole radius from 350 nm to 500 nm reduces the distance from the aC-film/vacuum interface where fringes are visible.

The close-to-focus ZPP-TEM image obtained with a graded ZPP with a $0.5/1.5 \mu\text{m}$ hole radius (Figure 5B) and the corresponding intensity profile (Figure 5E) show an efficient reduction of fringing due to the $1\text{-}\mu\text{m}$ -wide thickness gradient at the PP edge. The first maximum in the vacuum region and the first minimum in the aC-film region have the same intensity as in the conventional ZPP-TEM image (cf. Figure 5A and D) but further intensity oscillations are strongly damped. The reduction of fringing is even more pronounced in the close-to-focus ZPP-TEM image in Figure 5C and the corresponding intensity profile in Figure 5F that were obtained with a graded ZPP with $0.6/1.5 \mu\text{m}$ hole radius. The slightly larger ZPP hole further reduces the fringing periodicity to 6.5 nm (0.15 nm^{-1}) as expected for the $0.6\text{-}\mu\text{m}$ hole radius with a cut-on frequency of 0.14 nm^{-1} . The reduction of fringing in Figure 5C compared to Figure 5B can also be attributed to the smooth thickness profile of the $0.6/1.5 \mu\text{m}$ PP (yellow profile in Figure 2I) as compared to the thickness profile of the $0.5/1.5 \mu\text{m}$ PP with a kink at the hole edge (blue profile in Figure 2H). ZPP-TEM images were also acquired at $\Delta f = -200$ and -500 nm with extracted intensity line profiles included in Figures 5D–F, which essentially agree with the close-to-focus data. The simulated ZPP-TEM images (Figure 5G–I) and intensity line profiles (Figure 5J–L) agree well with the experimental data and confirm the reduction of fringing by the application of graded ZPPs. The results presented in Figure 5 demonstrate that a thickness gradient, which extends over a width of $1 \mu\text{m}$, efficiently reduces fringing in ZPP-TEM images. Fringing is strongly damped except for the asymmetric intensity oscillations directly at the edge of the aC-film.

Power spectra are shown in the experimental ZPP-TEM images in Figures 4 and 5. No distortions are visible and we expect that only minor distortions, if any, are present.

3.2 | Analysis of fringing in graded-ZPP-TEM images of a CNT bundle

In the following, we present an application of phase-contrast TEM using graded ZPPs. CNT bundles were chosen as interesting nanoscaled objects. The conventional TEM image obtained without PP (Figure 6A) shows CNT bundles dispersed on a holey aC film. We note that the CNTs protrude at an oblique angle into the vacuum region

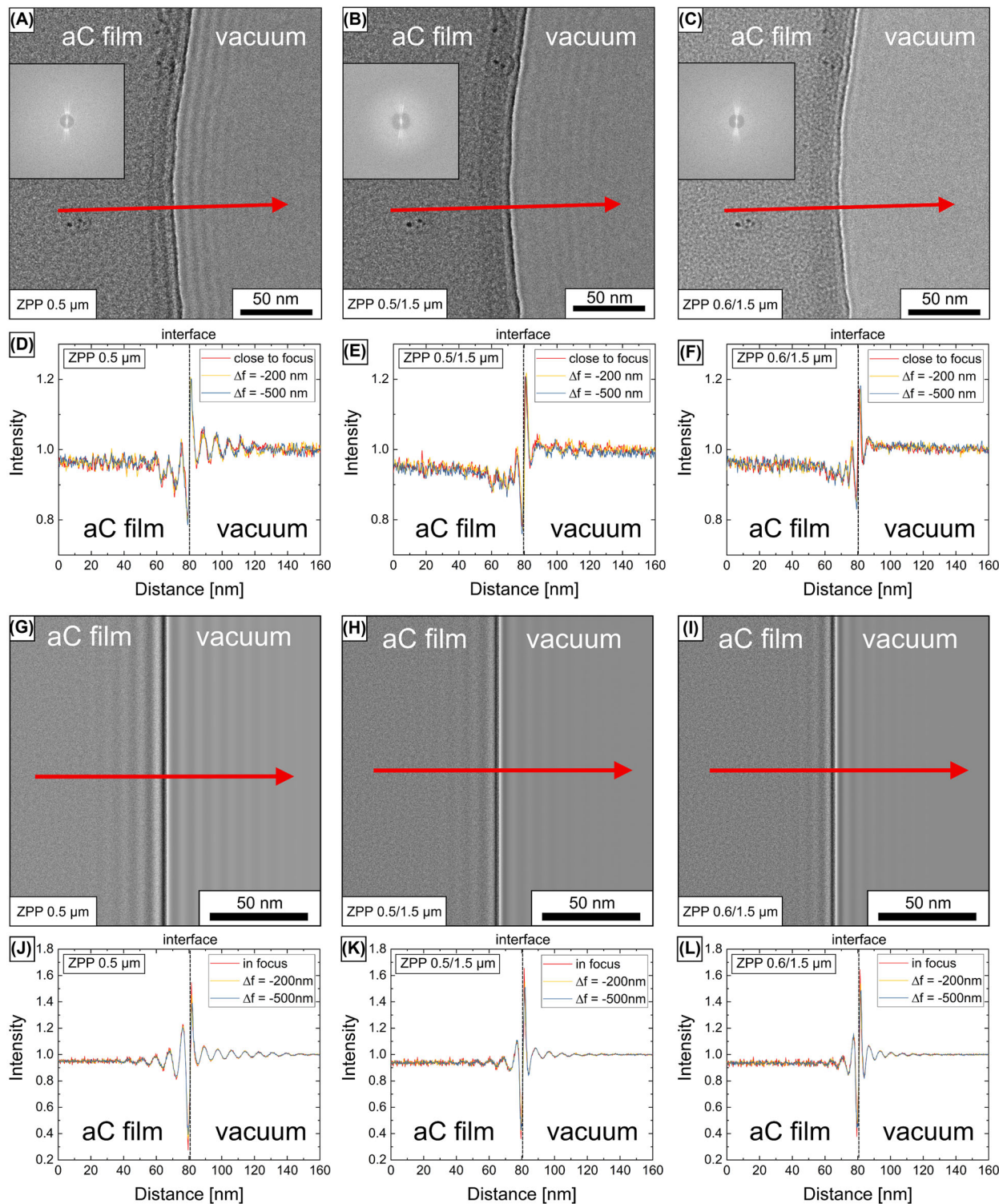


FIGURE 5 Experimental and simulated ZPP-TEM images of an aC-film/vacuum-interface region and corresponding intensity line profiles. Experimental ZPP-TEM images taken close to focus with (A) a conventional ZPP with a hole radius of $0.5\ \mu\text{m}$, (B) a graded ZPP with a hole radius of $0.5/1.5\ \mu\text{m}$ and (C) a graded ZPP with a hole radius of $0.6/1.5\ \mu\text{m}$ including corresponding power spectra. (D–F) Intensity profiles along the red arrows in the corresponding experimental TEM images A–C. Simulated in-focus ZPP-TEM images with (G) a conventional ZPP with a hole radius of $0.5\ \mu\text{m}$, (H) a graded ZPP with a hole radius of $0.5/1.5\ \mu\text{m}$ and (I) a graded ZPP with a hole radius of $0.6/1.5\ \mu\text{m}$. (J–L) Intensity profiles along the red arrows in the corresponding simulated TEM images G–I. The yellow and blue lines in D–F and J–L correspond to intensity profiles obtained at the same sample region from PP-TEM images taken with a defocus of $-200\ \text{nm}$ and $-500\ \text{nm}$. The intensity profiles are normalised with respect to the mean vacuum intensity in the corresponding image

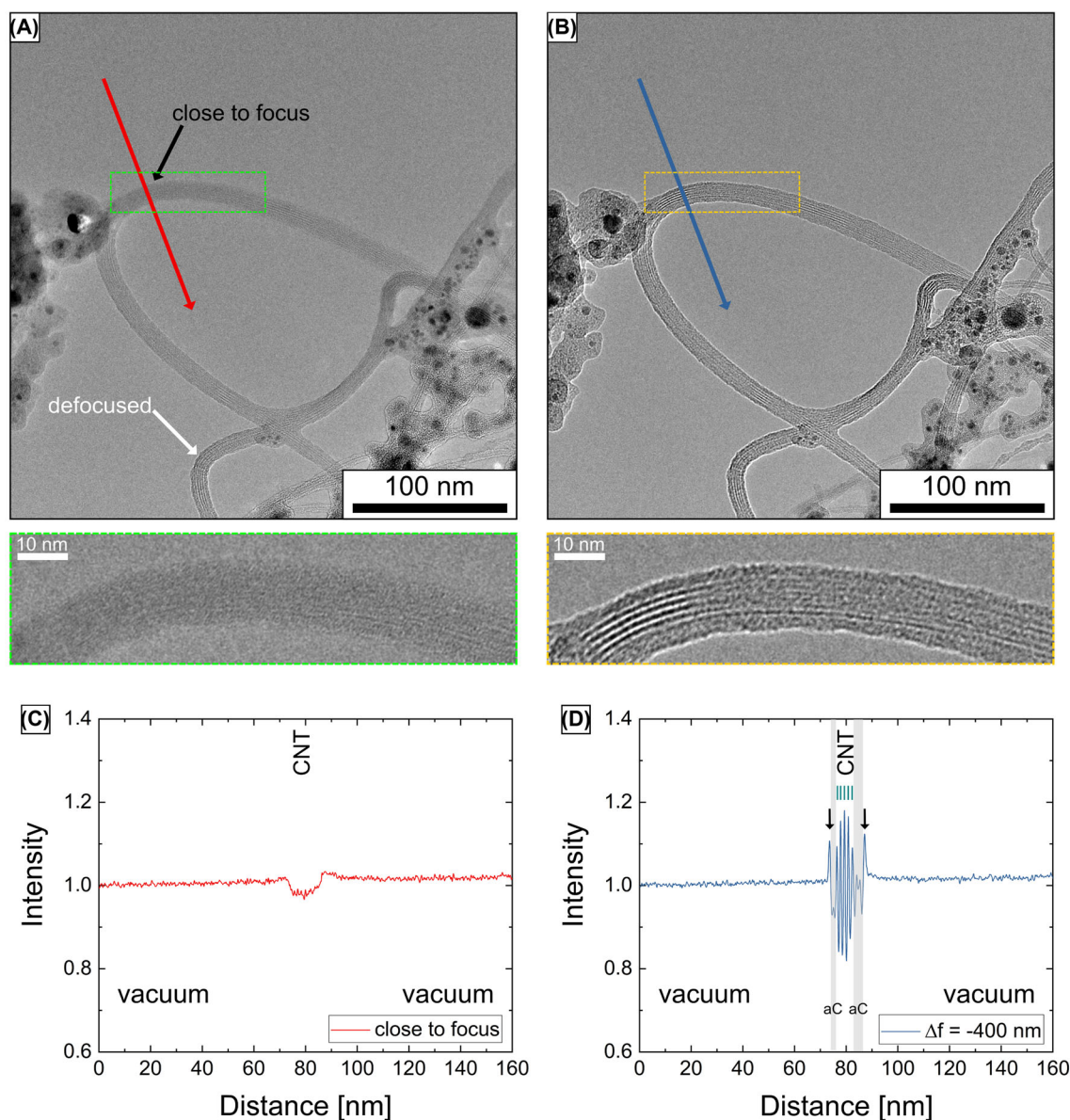


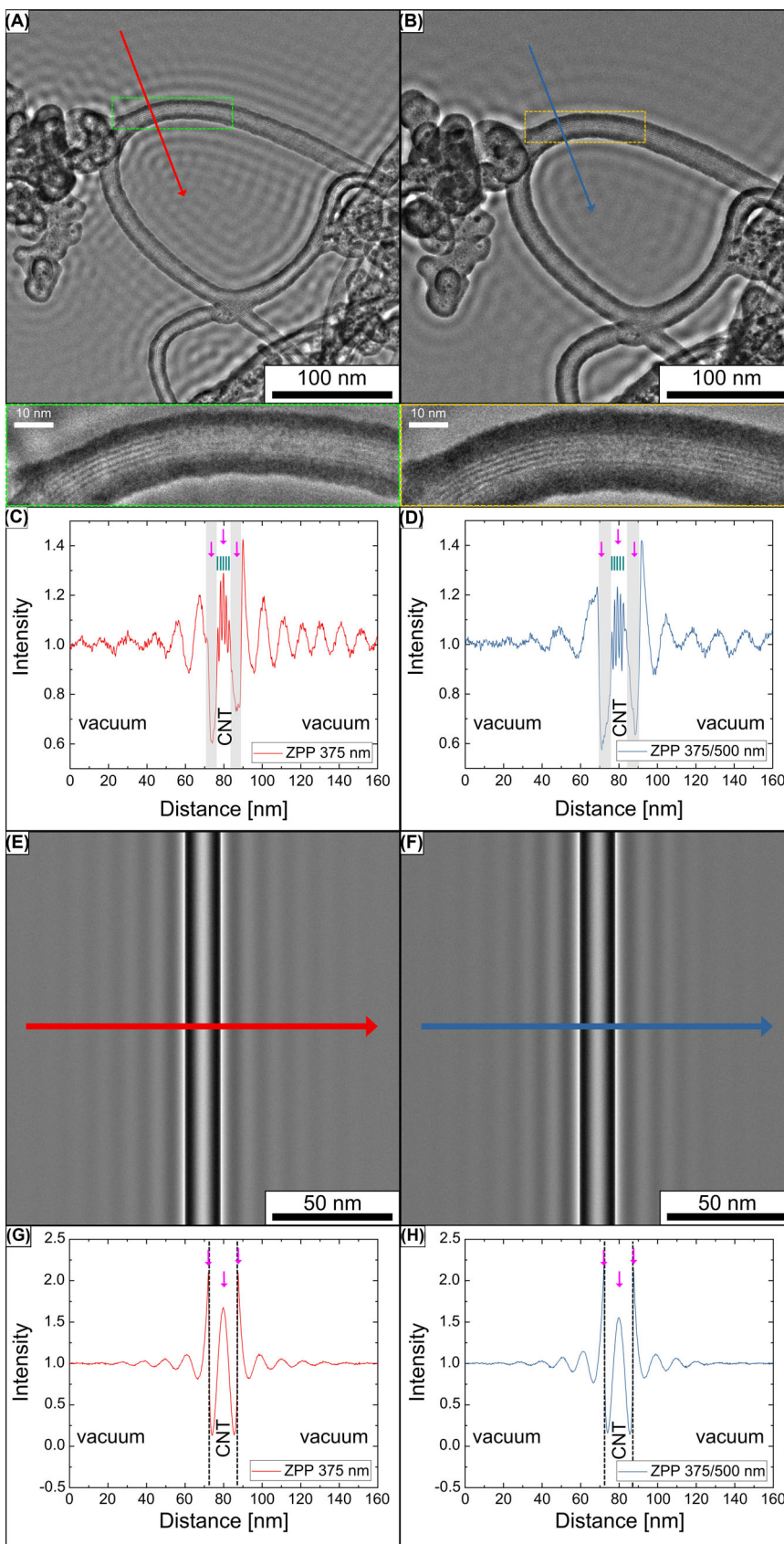
FIGURE 6 Conventional TEM images taken without PP (A) close to focus for the CNT bundle marked by a black arrow and (B) at a defocus of -400 nm. The green and yellow frames in A and B mark enlarged views of the analysed CNT bundle shown below A and B. The CNT bundles are located on different height levels and are partly defocused, for example, the CNT bundle marked by a white arrow. (C) Intensity line profile across the CNT bundle in A (red arrow) and (D) across the CNT bundle in B (blue arrow). The intensity profiles are normalised with respect to the mean vacuum intensity in the corresponding image. The black arrows in D mark Fresnel fringes. Blue-green lines indicate single CNTs with a distance of 1.6 nm within the bundle

of a hole. Thus, the CNT bundles are located at different positions in electron-beam direction leading to a defocus change along the CNT bundles. For alignment, we used the amorphous material in the left part of Figure 6A and the Thon rings in the associated live power spectrum to maintain a constant focus value for all images of the series. Following this procedure, the upper CNT bundle (marked by a black arrow) is close to focus, while another CNT bundle is defocused (marked by a white arrow). The upper close-to-focus CNT bundle is enlarged and displayed in the

green frame below, which does not allow to clearly resolve single CNTs in the bundle. This observation is confirmed by the intensity profile in Figure 6C (acquired along the red arrow in Figure 6A), which reveals only the contours of the CNT bundle. Applying a defocus of -400 nm (cf. conventional TEM image in Figure 6B and intensity profile Figure 6D along the blue arrow in Figure 6B) leads to phase contrast and clear resolution of single CNTs within the bundle, which appear as equidistant fringes with a distance of 1.6 nm in the intensity profile (blue-green lines in

FIGURE 7 Experimental close-to-focus ZPP-TEM images taken with (A) a conventional ZPP with a hole radius of 375 nm and (B) a graded ZPP with a hole radius of 375/500 nm. The green and yellow rectangles mark enlarged views of a CNT bundle, which are presented below.

Experimental intensity profiles (C) across the CNT bundle in A (red arrow) and (D) across the CNT bundle in B (blue arrow). Simulated in-focus ZPP-TEM images assuming (E) a conventional ZPP with a hole radius of 375 nm and (F) a graded ZPP with a hole radius of 375/500 nm. Simulated intensity profiles (G) across the CNT bundle in E (red arrow) and (H) across the CNT bundle in F (blue arrow). The magenta arrows mark fringing within the bundles. Blue-green lines indicate single CNTs within the bundle. The intensity profiles are normalised with respect to the mean vacuum intensity in the corresponding image



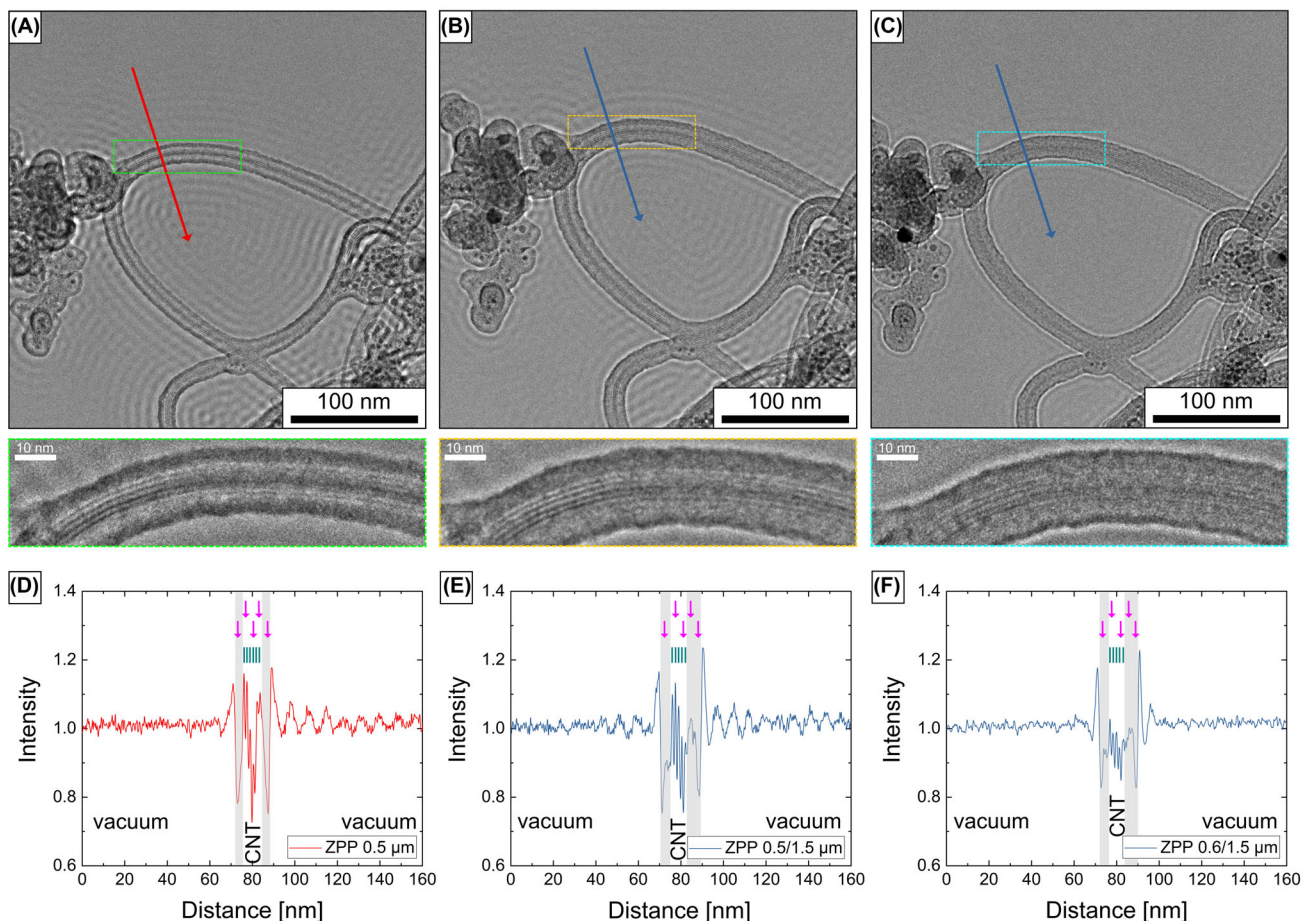


FIGURE 8 Experimental PP-TEM images taken close to focus with (A) a conventional ZPP with a hole radius of $0.5\ \mu\text{m}$, (B) a graded ZPP with a hole radius of $0.5/1.5\ \mu\text{m}$ and (C) a graded ZPP with a hole radius $0.6/1.5\ \mu\text{m}$. The green, yellow and blue rectangles mark regions, which are shown with higher magnification below A, B and C. Intensity line profiles across the CNT bundle (D) along the red arrow in A, (E) along the blue arrow in B and (F) along the blue arrow in C. The magenta arrows in D–F mark intensity maxima induced by fringing. The blue-green lines indicate equidistant fringes ($\sim 1.6\ \text{nm}$) related to single CNTs within the bundle. The intensity profiles are normalised with respect to the mean vacuum intensity in the corresponding image

Figure 6D). The measured fringe distance is in good agreement with previously published CNT-bundle properties.³¹ A distinct bright Fresnel fringe is visible around the CNT bundles (marked by black arrows in Figure 6D). We also note that the CNT bundle is covered by amorphous material, which is also visible in the intensity profile (grey regions in Figure 6D).

The experimental phase-contrast TEM images in Figure 7 were obtained under close-to-focus conditions as in Figure 6A, but with a conventional ZPP with a hole radius of $375\ \text{nm}$ in Figure 7A and a graded ZPP with a hole radius of $375/500\ \text{nm}$ in Figure 7B. Intensity line profiles along the red and blue arrows are shown in Figure 7C and D. The CNT bundle appears with clearly enhanced contrast in both images compared to the close-to-focus image in Figure 6A due to the additional phase contrast induced by the phase shift of the ZPP. However, fringing induced by the ZPP is observed to emanate from the

CNT-bundle/vacuum interface in Figure 7A and B with fringe distances corresponding to the cut-on frequency of the ZPPs. It is obvious that fringing is damped faster with increasing distance from the CNT bundle in the image in Figure 7B. The enlarged images of the CNT bundles within the green and yellow frames in Figure 7A and B reveal equidistant intensity oscillations induced by single CNTs. The enlarged views also show that the CNT bundle in Figure 7B has a slightly larger diameter ($1\text{--}2\ \text{nm}$), which can be assigned to contamination growth during image acquisition. Fringing leads to diffuse bright and dark contrast features within the CNT bundles (cf. Figure 7A and B and magenta arrows in the intensity profiles in Figure 7C and D), which is absent in Figure 6A and B taken without ZPP. Figure 7E and F shows corresponding image simulations and intensity line profiles in Figure 7G and H. The simulations are based on the simplified OWF in Figure 3B, which does not account for individual CNTs

in the bundle and the amorphous carbon contamination. However, the coarser features, that is, the broad bright fringe in the centre and the dark fringes at the CNT boundaries, are well reproduced. The simulations in Figure 7G and H also show the decay of fringing in the vacuum region, which is more pronounced for the graded ZPP.

The effect of differently graded ZPPs on fringing is illustrated in Figure 8. Figure 8A shows a close-to-focus ZPP image of CNT bundles obtained with a 0.5- μm -radius conventional ZPP with pronounced fringing. Fringing is strongly reduced in the images acquired with graded ZPPs with 0.5/1.5 μm and 0.6/1.5 μm hole radii (cf. Figure 8B and C). Magnified image sections reveal the contrast within the CNT bundle more clearly, where single CNTs are well resolved. In addition, three diffuse dark and two bright fringes are observed within the CNT bundle (magenta arrows in the intensity profiles in Figure 8D–F). The intensity profiles extracted from the graded ZPP images (Figure 8E and F) clearly show the reduction of fringing, which almost vanishes for the 0.6/1.5- μm ZPP. While shallow thickness gradients are preferable for the reduction of fringing, they will reduce the phase contrast of structures with spatial frequencies within the thickness gradient because the phase shift is reduced. Instead of a fixed cut-on frequency, a ‘soft’ cut-on-frequency range applies for a graded ZPP, comparable to an electrostatic Zach PP.³² However, imaging of single CNTs with a spatial frequency of 0.625 nm^{-1} is not degraded because the upper limit of the cut-on frequency range is 0.3518 nm^{-1} for the 0.5/1.5 μm and 0.6/1.5 ZPPs.

4 | CONCLUSIONS

We showed that Zernike phase plates (ZPPs) with a thickness gradient around the centre hole strongly reduce intensity oscillations around imaged objects denoted as fringing. The reduction of fringing depends on the inner radius of the ZPP hole and the thickness gradient around the hole. Depending on the spatial frequency spectrum of the imaged objects and the desired reduction of fringing, thickness gradient and inner hole radius can be optimised by controlled fabrication using Ga-ion focused-ion-beam milling. It is advisable to fabricate graded ZPPs with different hole diameters and gradients in one aC film to avoid an exchange of the aC film when different objects are investigated. By measuring the thickness profile around the ZPP hole, we showed that the reduction of fringing is most pronounced for ZPPs with a smooth and shallow thickness profile around the hole. Any thickness discontinuities, like kinks, should be avoided. Knowledge of the ZPP-thickness profile and the corresponding phase-shift distribution is also essential for image simulations, which are

in good agreement with experimental ZPP-TEM images of carbon nanotube bundles and the amorphous-carbon-film/vacuum interface of a test sample.

ACKNOWLEDGEMENTS


The authors acknowledge funding of this project by the German Research Foundation (Deutsche Forschungsgemeinschaft) under contract Ge 841/26. This work is supported by the Deutsche Forschungsgemeinschaft (DFG, German Research Foundation) under Germany’s Excellence Strategy – 2082/1–390761711 and by the Carl Zeiss Foundation. S.H. acknowledges funding from the German Research Foundation (HE 7675/1-1) and from the European Union’s Horizon 2020 research and innovation program under the Marie Skłodowska-Curie grant agreement No 889546.

Open access funding enabled and organized by Projekt DEAL.

ORCID

M. Obermair  <https://orcid.org/0000-0001-5503-8303>

S. Hettler  <https://orcid.org/0000-0002-9102-7895>

M. Hugenschmidt  <https://orcid.org/0000-0001-5020-9302>

REFERENCES

- Scherzer, O. (1949). The theoretical resolution limit of the electron microscope. *Journal of Applied Physics*, 20, 20–29. <https://doi.org/10.1063/1.1698233>
- Glaeser, R. M. (2013). Invited review article: Methods for imaging weak-phase objects in electron microscopy. *Review of Scientific Instruments*, 84, 111101. <https://doi.org/10.1063/1.4830355>
- Malac, M., Hettler, S., Hayashida, M., Kano, E., Egerton, R. F., & Beleggia, M. (2021). Phase plates in the transmission electron microscope: Operating principles and applications. *Microscopy (Oxford)*, 70, 75–115. <https://doi.org/10.1093/jmicro/dfaa070>
- Schwartz, O., Axelrod, J. J., Campbell, S. L., Turnbaugh, C., Glaeser, R. M., & Müller, H. (2019). Laser phase plate for transmission electron microscopy. *Nature Methods*, 16, 1016–1020. <https://doi.org/10.1038/s41592-019-0552-2>
- Müller, H., Jin, J., Danev, R., Spence, J., Padmore, H., & Glaeser, R. M. (2010). Design of an electron microscope phase plate using a focused continuous-wave laser. *New Journal of Physics*, 12, 73011. <https://doi.org/10.1088/1367-2630/12/7/073011>
- Zernike, F. (1942). Phase contrast, a new method for the microscopic observation of transparent objects. *Physica*, 9, 686–698. [https://doi.org/10.1016/S0031-8914\(42\)80035-X](https://doi.org/10.1016/S0031-8914(42)80035-X)
- Danev, R., & Nagayama, K. (2001). Transmission electron microscopy with Zernike phase plate. *Ultramicroscopy*, 88, 243–252. [https://doi.org/10.1016/S0304-3991\(01\)00088-2](https://doi.org/10.1016/S0304-3991(01)00088-2)
- Boersch, H. (1947). Über die Kontraste von Atomen im Elektronenmikroskop. *Zeitschrift für Naturforschung*, 2a, 615–633.
- Willasch, D. (1975). High-resolution electron microscopy with profiled phase plates. *Optik*, 44, 17–36.
- Wanner, M., Bach, D., Gerthsen, D., Werner, R., & Tesche, B. (2006). Electron holography of thin amorphous carbon films: Measurement of the mean inner potential and a thickness-

- independent phase shift. *Ultramicroscopy*, *106*, 341–345. <https://doi.org/10.1016/j.ultramic.2005.10.004>
11. Danov, K., Danev, R., & Nagayama, K. (2000). Electric charging of thin films measured using the contrast transfer function. *Ultramicroscopy*, *87*, 45–54. [https://doi.org/10.1016/S0304-3991\(00\)00061-9](https://doi.org/10.1016/S0304-3991(00)00061-9)
 12. Danov, K., Danev, R., & Nagayama, K. (2002). Reconstruction of the electric charge density in thin films from the contrast transfer function measurements. *Ultramicroscopy*, *90*, 85–95. [https://doi.org/10.1016/S0304-3991\(01\)00143-7](https://doi.org/10.1016/S0304-3991(01)00143-7)
 13. Hettler, S., Dries, M., Hermann, P. M., Gerthsen, D., & Malac, M. (2017). Carbon contamination in scanning transmission electron microscopy and its impact on phase-plate applications. *Micron (Oxford, England: 1993)*, *96*, 38–47. <https://doi.org/10.1016/j.micron.2017.02.002>
 14. Hettler, S., Kano, E., Dries, M., Gerthsen, D., Pfaffmann, L., Bruns, M., & Malac, M. (2018). Charging of carbon thin films in scanning and phase-plate transmission electron microscopy. *Ultramicroscopy*, *184*, 252–266. <https://doi.org/10.1016/j.ultramic.2017.09.009>
 15. Danev, R., Glaeser, R. M., & Nagayama, K. (2009). Practical factors affecting the performance of a thin-film phase plate for transmission electron microscopy. *Ultramicroscopy*, *109*, 312–325. <https://doi.org/10.1016/j.ultramic.2008.12.006>
 16. Marko, M., Meng, X., Hsieh, C., Roussie, J., & Striemer, C. (2013). Methods for testing Zernike phase plates and a report on silicon-based phase plates with reduced charging and improved ageing characteristics. *Journal of Structural Biology*, *184*, 237–244. <https://doi.org/10.1016/j.jsb.2013.08.008>
 17. Dries, M., Obermair, M., Hettler, S., Hermann, P., Seemann, K., Seifried, F., & Gerthsen, D. (2018). Oxide-free aC/Zr0.65Al0.075Cu0.275/aC phase plates for transmission electron microscopy. *Ultramicroscopy*, *189*, 39–45. <https://doi.org/10.1016/j.ultramic.2018.03.003>
 18. Edgcombe, C. J. (2015). Effects of low-spatial-frequency response of phase plates on TEM imaging. *Journal of Physics: Conference Series*, *644*, 12031. <https://doi.org/10.1088/1742-6596/644/1/012031>
 19. Danev, R., & Nagayama, K. (2011). Optimizing the phase shift and the cut-on periodicity of phase plates for TEM. *Ultramicroscopy*, *III*, 1305–1315. <https://doi.org/10.1016/j.ultramic.2011.04.004>
 20. Kishchenko, G. P., Danev, R., Fisher, R., He, J., Hsieh, C., Marko, M., & Sui, H. (2015). Effect of fringe-artifact correction on subtomogram averaging from Zernike phase-plate cryo-TEM. *Journal of Structural Biology*, *191*, 299–305. <https://doi.org/10.1016/j.jsb.2015.07.009>
 21. Kurth, P., Pattai, S., Rudolph, D., Overbuschmann, J., Wamser, J., & Irsen, S. (2014). Artifact-free, long-lasting phase plate. *MAM*, *20*, 220–221. <https://doi.org/10.1017/S1431927614002827>
 22. Volkenandt, T., Müller, E., & Gerthsen, D. (2014). Sample thickness determination by scanning transmission electron microscopy at low electron energies. *Microscopy and Microanalysis*, *20*, 111–123. <https://doi.org/10.1017/S1431927613013913>
 23. Pretzsch, R., Dries, M., Hettler, S., Spiecker, M., Obermair, M., & Gerthsen, D. (2019). Investigation of hole-free phase plate performance in transmission electron microscopy under different operation conditions by experiments and simulations. *Advanced Structural and Chemical Imaging*, *5*, 20. <https://doi.org/10.1186/s40679-019-0067-z>
 24. Hettler, S., Wagner, J., Dries, M., Oster, M., Wacker, C., Schröder, R. R., & Gerthsen, D. (2015). On the role of inelastic scattering in phase-plate transmission electron microscopy. *Ultramicroscopy*, *155*, 27–41. <https://doi.org/10.1016/j.ultramic.2015.04.001>
 25. Barthel, J., & Thust, A. (2010). Aberration measurement in HRTEM: Implementation and diagnostic use of numerical procedures for the highly precise recognition of diffractogram patterns. *Ultramicroscopy*, *III*, 27–46. <https://doi.org/10.1016/j.ultramic.2010.09.007>
 26. Tonomura, A. (1999). *Electron holography* (2nd, Enlarged ed.), Berlin, Heidelberg: Springer Berlin Heidelberg, s.l.
 27. Dries, M., Hettler, S., Schulze, T., Send, W., Müller, E., Schneider, R., & Samwer, K. (2016). Thin-film phase plates for transmission electron microscopy fabricated from metallic glasses. *Microscopy and Microanalysis*, *22*, 955–963. <https://doi.org/10.1017/S143192761601165X>
 28. Coene, W., Thust, A., op de Beeck, M., & van Dyck, D. (1996). Maximum-likelihood method for focus-variation image reconstruction in high resolution transmission electron microscopy. *Ultramicroscopy*, *64*, 109–135. [https://doi.org/10.1016/0304-3991\(96\)00010-1](https://doi.org/10.1016/0304-3991(96)00010-1)
 29. Hettler, S., & Arenal, R. (2021). Comparative image simulations for phase-plate transmission electron microscopy. *Ultramicroscopy*, *227*, 113319. <https://doi.org/10.1016/j.ultramic.2021.113319>
 30. Obermair, M., Hettler, S., Hsieh, C., Dries, M., Marko, M., & Gerthsen, D. (2020). Analyzing contrast in cryo-transmission electron microscopy: Comparison of electrostatic Zach phase plates and hole-free phase plates. *Ultramicroscopy*, *218*, 113086. <https://doi.org/10.1016/j.ultramic.2020.113086>
 31. Thess, L., Nikolaev, D., Petit, R., Xu, K., Rinzler, C., Scuseria, T., & Fischer, S. (1996). Crystalline ropes of metallic carbon nanotubes. *Science*, *273*, 483–487. <https://doi.org/10.1126/science.273.5274.483>
 32. Hettler, S., Gamm, B., Dries, M., Frindt, N., Schröder, R. R., & Gerthsen, D. (2012). Improving fabrication and application of zach phase plates for phase-contrast transmission electron microscopy. *Microscopy and Microanalysis*, *18*, 1010–1015. <https://doi.org/10.1017/S1431927612001560>

SUPPORTING INFORMATION

Additional supporting information may be found in the online version of the article at the publisher's website.

How to cite this article: Obermair, M., Hettler, S., Dries, M., Hugenschmidt, M., Spiecker, R., & Gerthsen, D. (2022). Carbon-film-based Zernike phase plates with smooth thickness gradient for phase-contrast transmission electron microscopy with reduced fringing artefacts. *Journal of Microscopy*, *287*, 45–58. <https://doi.org/10.1111/jmi.13108>